ARTICLES
https://doi.org/10.1038/s41928-020-0429-5
nature electronics

Check for updates

An aquatic-vision-inspired camera based on a monocentric lens and a silicon nanorod photodiode array

Minsung Kim[1,2,7], Gil Ju Lee[3,7], Changsoon Choi[1,2,7], Min Seok Kim[3,7], Mincheol Lee[1,2], Siyi Liu[4], Kyoung Won Cho[1,2], Hyun Myung Kim[3], Hyojin Cho[1,2], Moon Kee Choi[5], Nanshu Lu[4], Young Min Song[3]✉ and Dae-Hyeong Kim[1,2,6]✉

Conventional wide-field-of-view cameras consist of multi-lens optics and flat image sensor arrays, which makes them bulky and heavy. As a result, they are poorly suited to advanced mobile applications such as drones and autonomous vehicles. In nature, the eyes of aquatic animals consist of a single spherical lens and a highly sensitive hemispherical retina, an approach that could be beneficial in the development of synthetic wide-field-of-view imaging systems. Here, we report an aquatic-vision-inspired camera that consists of a single monocentric lens and a hemispherical silicon nanorod photodiode array. The imaging system features a wide field of view, miniaturized design, low optical aberration, deep depth of field and simple visual accommodation. Furthermore, under vignetting, the photodiode array enables high-quality panoramic imaging due to the enhanced photodetection properties of the silicon nanorod photodiodes.

Miniaturized, lightweight cameras that offer a wide field of view (FoV) are of use in applications that require object tracking capabilities, such as drones and autonomous vehicles[1,2]. However, due to the large Petzval field curvature in wide FoV imaging, a large number of lenses are required to focus panoramic scenes onto a flat image sensor array[3,4]. For example, a typical wide-angle camera module, which has a FoV of over 120°, requires between 8 and 13 lenses[5]. This dramatically increases the overall volume and weight of the camera module[3] (Supplementary Fig. 1).

Biological imaging systems have been optimized through evolution and have inspired the development of biomimetic cameras[6–8]. Curved image sensor arrays that mimic the human eye using single plano-convex lenses have, for example, enabled imaging with fewer optical aberrations (Supplementary Fig. 2a)[9–11]. However, these human-eye-inspired cameras offer limited FoVs of less than 100° due to off-axis aberrations, particularly at large angles (Supplementary Fig. 2b)[3]. In addition, the natural human eye does not use single-lens optics as it cannot reduce optical aberrations without its cornea, which serves as an additional refractive lens (Supplementary Fig. 2c)[12]. Alternatively, compound eye-type imaging systems inspired by arthropod eyes have demonstrated wide-FoV characteristics (Supplementary Fig. 3a)[13–16]. However, the visual acuity (clarity of vision) of compound eyes is inferior to that of camera-type eyes, such as vertebrate and aquatic animal eyes, because their corneal microlens cannot be miniaturized to have a sufficient diffraction limit (Supplementary Fig. 3b).

Aquatic-type vision, found in fish[17], cephalopods[18] and aquatic mammals[19], features a wide FoV of up to 160°, high visual acuity, minimal optical aberrations[18], deep depth of field (DoF)[20] and simple visual accommodation[21], all in small form factors[5]. Furthermore, photoreceptors on the retinas of aquatic eyes are highly light-sensitive, which allows high visual acuity even in dim underwater conditions[22]. Many of these characteristics are a consequence of a single spherical monocentric lens with a parabolic refractive index (RI) profile[5,17] and a hemispherical curved retina with highly light-sensitive rod cells[23]. These features have inspired the development of wide-FoV cameras that meet key requirements for advanced mobile electronics[24,25].

In this Article, we report a bio-inspired camera that adopts the unique optical advantages of aquatic vision by integrating a monocentric lens and a hemispherical silicon nanorod photodiode array (h-SiNR-PDA). The nanorod photodiode array has a textured and passivated structure that enhances its light sensitivity, providing improved imaging under vignetting. The aquatic-vision-inspired camera features a FoV of 120°, an 11.5-mm form factor, a DoF of 20 cm to infinity and minimal optical aberrations with simple accommodation.

Structural and functional features of aquatic vision in nature

Figure 1a presents a photograph of an aquatic animal (Cichlid), while the inset shows a corresponding schematic illustration demonstrating the anatomy of its eye. Aquatic vision features a wide FoV with clear visual acuity, even in a dim underwater environment, as a result of the single spherical monocentric lens and highly light-sensitive hemispherical retina[5,22]. The deep DoF and

[1]Center for Nanoparticle Research, Institute for Basic Science (IBS), Seoul, Republic of Korea. [2]School of Chemical and Biological Engineering, Institute of Chemical Processes, Seoul National University, Seoul, Republic of Korea. [3]School of Electrical Engineering and Computer Science, Gwangju Institute of Science and Technology, Gwangju, Republic of Korea. [4]Center for Mechanics of Solids, Structures and Materials, Department of Aerospace Engineering and Engineering Mechanics, Department of Biomedical Engineering, Texas Materials Institute, University of Texas at Austin, Austin, TX, USA. [5]School of Materials Science and Engineering, Ulsan National Institute of Science and Technology (UNIST), Ulsan, Republic of Korea. [6]Department of Materials Science and Engineering, Seoul National University, Seoul, Republic of Korea. [7]These authors contributed equally: Min Sung Kim, Gil Ju Lee, Changsoon Choi, Min Seok Kim. ✉e-mail: ymsong@gist.ac.kr; dkim98@snu.ac.kr

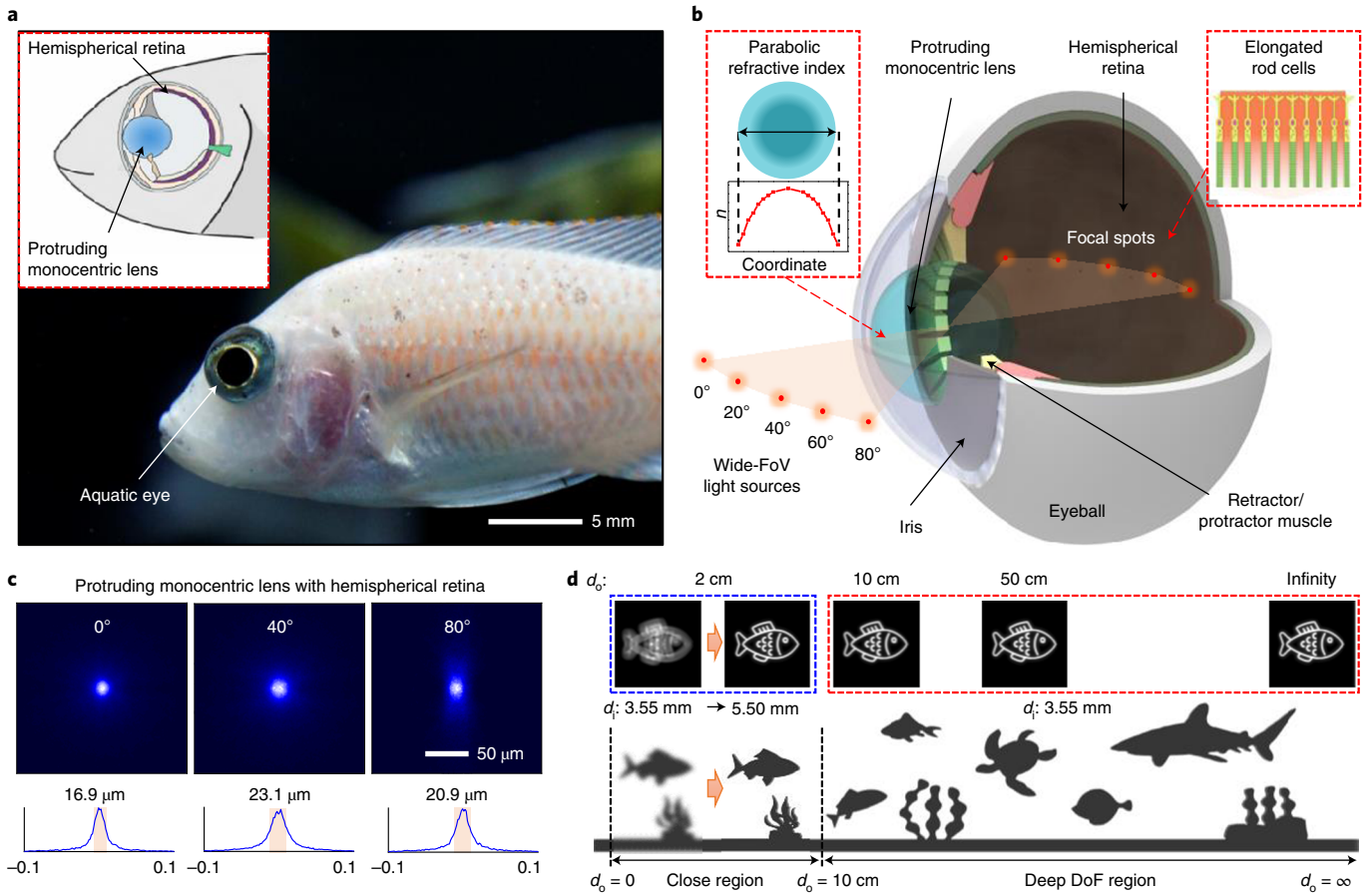

Fig. 1 | Structural and functional features of aquatic vision in nature. a, Photograph of an example Cichlid. Inset: an anatomical illustration of the aquatic eye. **b**, Schematic of the aquatic eye with its key features. Left inset: parabolic RI profile of the protruding monocentric lens. Right inset: highly sensitive elongated rod cells in the hemispherical retina. **c**, Optical simulation of light spots focused by the protruding monocentric lens (top) for light sources at three different angles (0°, 40° and 80°). The line graphs (bottom) show corresponding cross-sectional intensity profiles. **d**, The top frames show an optical simulation for focusing objects located at different d_o (for example, 2 cm in the blue dashed box; 10 cm, 50 cm and infinity in the red dashed box). The blurry image for the object located at $d_o = 2$ cm can be refocused by visual accommodation (that is, d_i change from 3.55 mm to 5.50 mm). The bottom frame shows a schematic drawing of the deep DoF.

facile visual accommodation are other unique advantages of aquatic vision[20]. In nature, such features protect aquatic animals from enemies and help in hunting prey. In the real world, if a similar imaging system were available, such features would be useful for obstacle avoidance and object tracking, particularly in advanced mobile electronics[1].

These optical properties arise from the unique structural and functional features of the aquatic eye: that is, a protruding monocentric lens, a hemispherical retina, an iris and retractor/protractor muscles (Fig. 1b). The protruding monocentric lens, with its spherical and symmetric shape, forms a hemispherical focal plane. By matching this focal plane with the hemispherical retina, aquatic vision achieves a wide FoV. In addition, the parabolic RI profile of the monocentric lens (Fig. 1b, left inset) minimizes optical aberrations, allowing nearly zero aberrations for panoramic scenes. The iris blocks stray light and minimizes optical aberrations further. Meanwhile, the retina contains elongated rod cells (Fig. 1b, right inset) that elongate the light path for better light absorption, and is thus suited to detecting low-intensity light in the dim undersea environment[22]. The retractor/protractor muscles move the monocentric lens back and forth for visual accommodation.

These characteristics (the wide FoV without optical aberrations, for example) can be confirmed theoretically by means of optical simulations. A three-dimensional (3D) ray-tracing simulation based on the Monte-Carlo method was used to validate the inherent superiority of the monocentric lens in wide-FoV imaging (Fig. 1c). The aquatic vision can focus light from wide angular directions (<160°) to within a tiny spot on the hemispherical retina, confirming the small coma aberration. The 2D ray-tracing simulation also supports the effective correction of off/on-axis aberrations by the monocentric lens (Supplementary Fig. 4). More details about the ray-tracing simulation are provided in Supplementary Note 1.

Aquatic vision also features a deep DoF resulting from its inherently short focal length, which enables well-focused imaging for objects located at a wide range of distances (Fig. 1d, bottom). A clear image is obtained when the image distance (d_i) is equal to the focal length (d_f) of the monocentric lens for an object located at the object distance (d_o) (Supplementary Fig. 5). In aquatic vision, all objects located at 10 cm or further are clearly imaged by the monocentric lens with $d_i = 3.55$ mm (red dashed box, Fig. 1d; deep DoF region). For closer objects (for example, located at 2 cm), the focal length becomes longer and the image captured with $d_i = 3.55$ mm becomes blurry. However, by slightly modulating d_i to be 5.50 mm using retractor/protractor muscles (Fig. 1b), the blurred image can be easily refocused (blue dashed box, Fig. 1d; close region). Visual accommodation in the aquatic eye is simpler than in the human

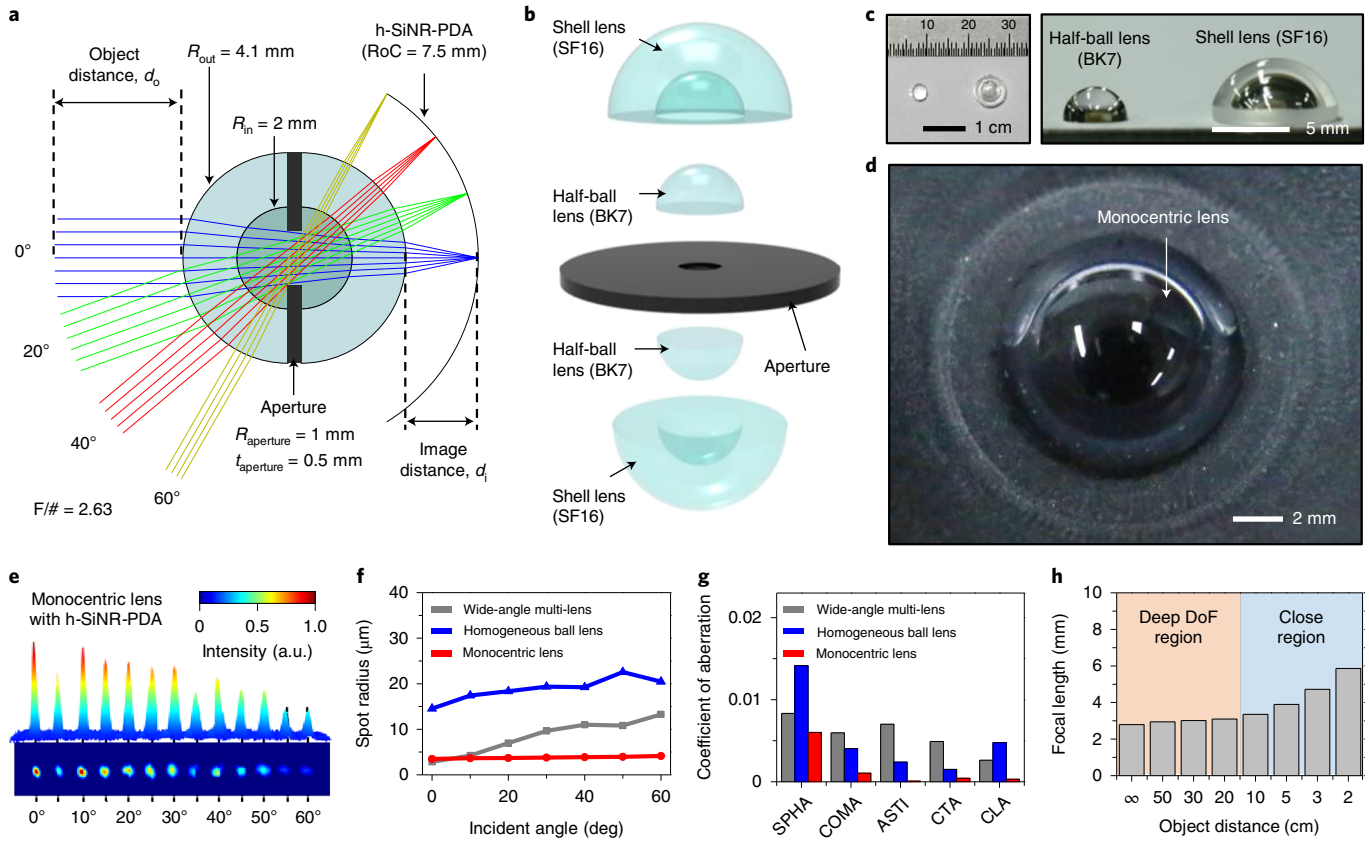

Fig. 2 | Monocentric lens inspired by the protruding monocentric lens of aquatic eyes. a, Ray-tracing simulation of the aquatic-vision-inspired camera. RoC, radius of curvature. **b**, Exploded schematic of the monocentric lens. **c**, Photographs showing a disassembled form of the monocentric lens. Top (left) and side (right) views of the inner half-ball lens (BK7) and the outer shell lens (SF16). **d**, Photograph showing an assembled form of the monocentric lens. **e**, Light intensity (top) and size (bottom) of laser spots for different incident angles, focused and detected by using the monocentric lens and h-SiNR-PDA, respectively. **f**, Optical simulation of the monochromic spot radius for different incident angles. **g**, Seidel aberration coefficients of the monocentric lens and control lenses. **h**, Focal lengths for objects at various distances, focused by the monocentric lens (deep DoF region, red; close region, blue).

eye in terms of optics, because it does not need any changes in the original lens shape (Supplementary Fig. 6a)[21] (visual accommodation in the human eye requires deformation of the lens; Supplementary Fig. 6b)[3].

Monocentric lens inspired by a natural protruding monocentric lens

An artificial imaging system inspired by the natural aquatic eye can be developed by integration of the monocentric lens and h-SiNR-PDA (Fig. 2a). The monocentric lens inspired by the protruding monocentric lens in the aquatic eye (Fig. 1) has a spherical and symmetric shape (Supplementary Fig. 7), where the half-ball lens (BK7) and shell lens (SF16) are assembled on both sides of the aperture using a transparent optical adhesive (NOA 61) (Fig. 2b). Such a symmetric hemispherical lens shape is helpful for eliminating undesired wavefront error. Photographs of the lenses and their assembled form are shown in Fig. 2c,d, respectively. Details of the fabrication process of the monocentric lens are provided in Supplementary Fig. 8 and the Methods.

Such a core–shell structure with two RI values in the monocentric lens (Fig. 2b) is inspired by the parabolic RI profile in the protruding monocentric lens of an aquatic eye (Fig. 1b, left inset). However, in the monocentric lens, the outer shell (SF16, $R_{out} = 4.1$ mm) is designed to have a larger RI ($n_{out} = 1.65$) than the inner core (BK7, $R_{in} = 2$ mm; $n_{in} = 1.52$) to achieve the small focal spot radius, because the imaging system is under air, not under water (Supplementary Fig. 9). The optimal RI difference of the lenses ($\Delta n = n_{out} - n_{in}$) and the radius ratio ($R_{in}/R_{out}$) are around 0.13 and 0.48, respectively (Supplementary Fig. 10). The aperture is placed at the centre of individual half-ball lenses to achieve the wide FoV without intensity attenuation of focused lights (Supplementary Fig. 11). With these optimizations, the monocentric lens with two RI values shows comparable (or better in some conditions) focusing capabilities than the natural protruding monocentric lens or the monocentric lens with three RI values (Supplementary Fig. 12). It also has advantages in terms of fabrication and cost compared to the recently developed lenses (for example, a lens with continuous RI[26] and a flat metalens[27]). More details about the design optimization of the monocentric lens are included in Supplementary Note 2.

The monocentric lens, when integrated with the h-SiNR-PDA inspired by the hemispherical retina of aquatic eyes (Fig. 1b), enables wide-FoV imaging. Because the curved shape of the h-SiNR-PDA is matched with the hemispherical focal plane (Fig. 2a), the monocentric lens effectively focuses the light from wide angular directions without off-axis aberrations, although vignetting (that is, light intensity attenuation at wide angles) is observed (Fig. 2e). On the other hand, significant blurring occurs, particularly at large angles, when a flat photodetector array (f-PDA) is used (Supplementary Fig. 13). In particular, the monochromatic spot radii of the monocentric lens are less than 4.2 μm for all incident angles (Fig. 2f and Supplementary Fig. 14); these are much smaller spot radii than

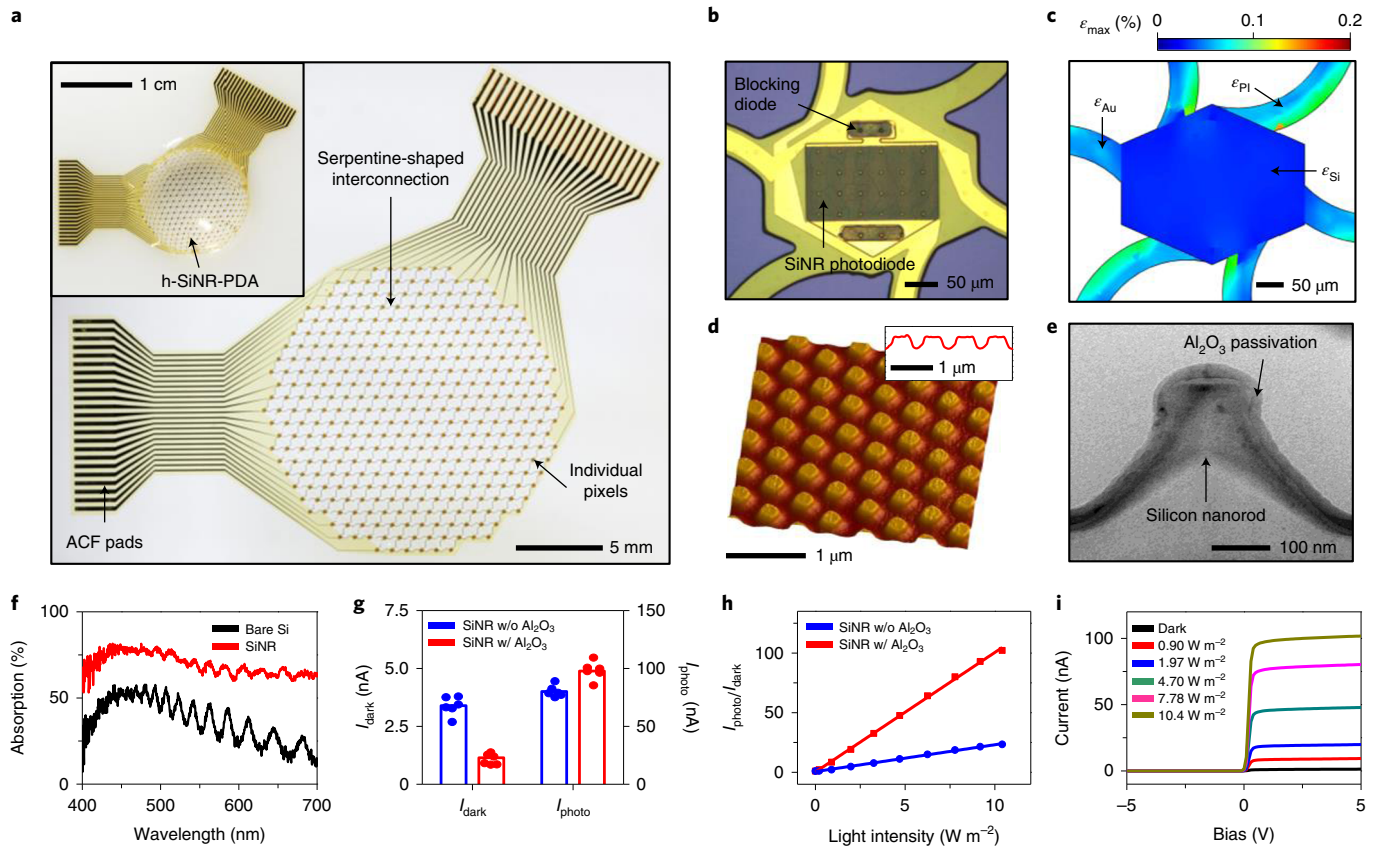

Fig. 3 | h-SiNR-PDA inspired by the retina of aquatic eyes. a, Photograph of the SiNR photodiode array fabricated on a flat substrate. ACF, anisotropic conductive film. Inset: photograph of the same array transferred to the hemispherical surface. **b**, Optical microscope image of an individual pixel composed of a photodiode and a blocking diode. **c**, FEA of the strain distribution in the individual pixel of the h-SiNR-PDA. **d**, Three-dimensional (3D) AFM image showing the surface morphology of the SiNRs. Inset: height profile of the SiNRs. **e**, Cross-sectional TEM image of the SiNRs. **f**, Photo-absorption profile of the bare silicon and SiNRs in the visible spectrum range. **g**, Statistical analysis ($N=6$) of I_{dark} and I_{photo} for the SiNR photodiode with and without Al_2O_3 passivation. **h**, Sensitivity (I_{photo}/I_{dark}) of the SiNR photodiode with and without Al_2O_3 passivation under illumination with various light intensities. **i**, *I*–*V* curves of the SiNR photodiode serially connected with the blocking diode under various light intensities.

those of a conventional wide-angle multi-lens or a homogeneous ball lens (Fig. 2f). Furthermore, the achromatic on/off-axis aberrations (for example, spherical aberration (SPHA), coma aberration (COMA), and astigmatism aberration (ASTI)) and chromatic aberrations (for example, chromatic transverse aberration (CTA) and chromatic longitudinal aberration (CLA)) of the monocentric lens are much smaller than those of the wide-angle multi-lens or homogeneous ball lens (Fig. 2g)[28]. More details about the optical aberration of the monocentric lens compared to control lenses are provided in Supplementary Note 3.

The monocentric lens also has a short d_f ranging between 2.79 mm and 5.87 mm, which enables deep DoF imaging. Figure 2h presents the d_f of the monocentric lens for objects located at various distances. The objects at more than 20 cm (20 cm to infinity) have almost similar d_f values around 2.95 mm (deep DoF region in Fig. 2h). Thus, those objects can be focused well by maintaining $d_{i,far} = 2.95$ mm (Supplementary Fig. 15a). When objects are closer ($d_o < 20$ cm), d_f gradually changes (close region in Fig. 2h) and the images become blurry (Supplementary Fig. 15b). However, accommodation can be applied easily in the aquatic eye using the retractor and protractor muscles (Fig. 1b). Such blurred images are easily refocused by slightly modulating d_i (Supplementary Fig. 15c,d). This is clearly simpler than the accommodation method of the conventional wide-angle multi-lens system, in which each distance between individual lenses has to be adjusted[3].

h-SiNR-PDA inspired by the retina of aquatic eyes

Inspired by the hemispherical retina with elongated rod cells in aquatic eyes (Fig. 1b and right inset), we developed the h-SiNR-PDA, a mesh-shaped 23 × 23-hexagonal-pixel array (Fig. 3a and inset). Individual devices, that is, the nanorod-textured silicon photodiode and blocking diode[13], are placed inside the hexagonal pixel (Fig. 3b), and connected as a lateral n–p–n configuration for passive matrix array operation (Supplementary Fig. 16)[29]. The detailed fabrication process for the h-SiNR-PDA is described in Supplementary Fig. 17 and the Methods, and cross-sectional schematic illustrations for the fabrication of an individual pixel are shown in Supplementary Fig. 18.

The mesh array design with serpentine interconnections minimizes induced strain on the array[30–32]. According to finite element analysis (FEA), induced strain on an individual photodiode is 0.02%, which is much lower than the fracture strain of silicon (~1%)[33] (Fig. 3c). The ultrathin thickness of the array (~5.5 μm), including the thin flexible silicon photodetecting layer (~1.25 μm), is helpful in enhancing the mechanical flexibility of the array[34,35]. The h-SiNR-PDA could thus be conformally laminated on a concavely hemispherical surface without mechanical fractures (Supplementary Fig. 19a). The pixel distribution at the perimeter of the h-SiNR-PDA is close to a circle, so the array can cover almost the entire hemispherical surface (Supplementary Fig. 19b). More details about the mechanical analysis are provided in Supplementary Note 4.

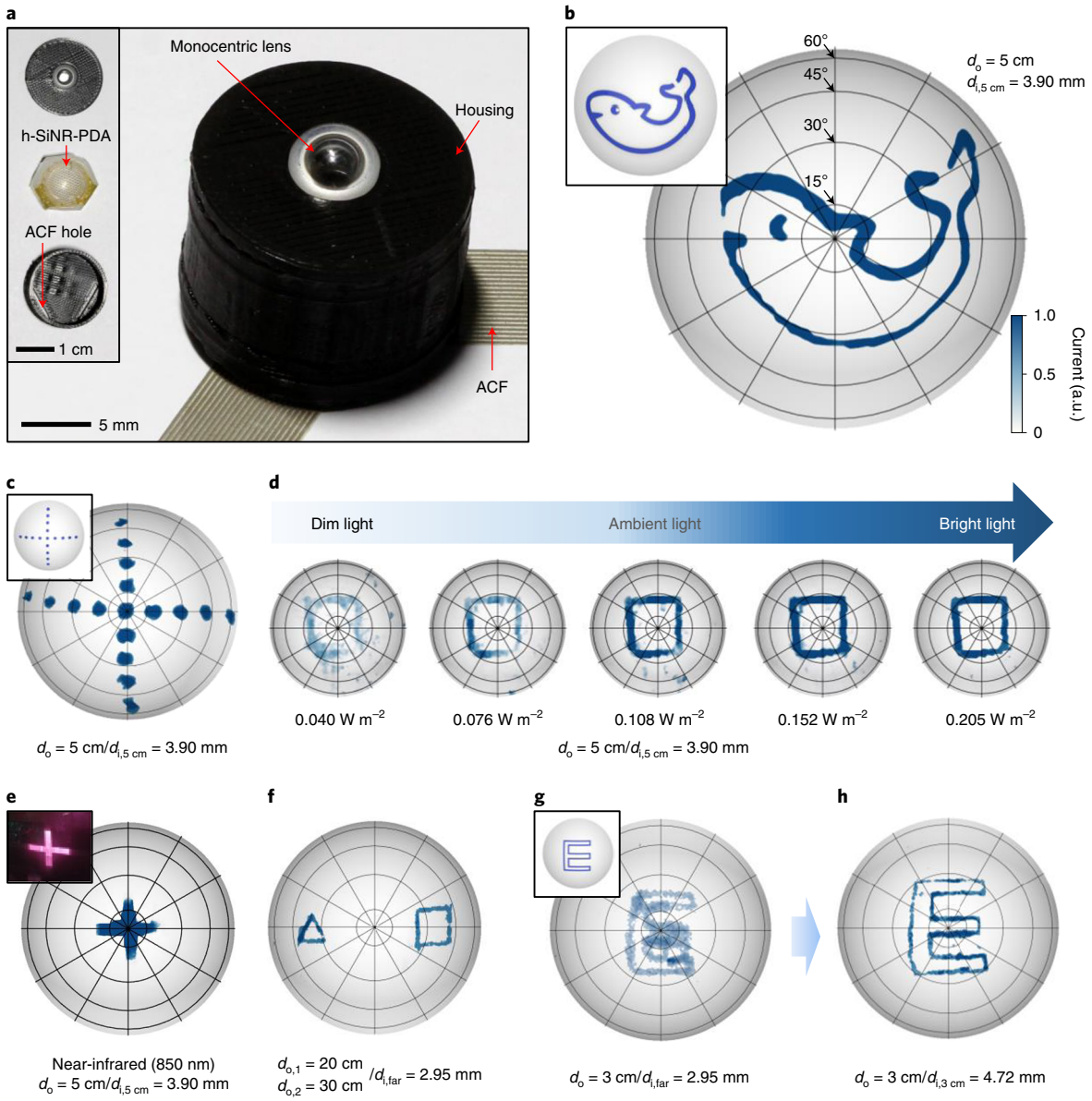

Fig. 4 | Imaging demonstration with the integrated camera module. a, Photograph of the assembled aquatic-vision-inspired camera module. Inset: its disassembled form. **b**, Panoramic imaging demonstration (FoV = 120°). Inset: the original object image. **c**, Wide-FoV imaging of a cross pattern composed of spots. The spots are located at various angles (−60° to ~60°). Inset: image of the original spotted cross pattern. **d**, Imaging demonstrations under different focused light intensities from 0.040 W m^{-2} to 0.205 W m^{-2}. **e**, NIR imaging demonstration (λ = 850 nm). Inset: the original NIR object image. **f**, Imaging demonstration for a triangle (object 1) and square (object 2) located at different distances ($d_{o,1}$ = 20 cm and $d_{o,2}$ = 30 cm) and at different angles with 90° difference. The image is captured with $d_{i,far}$ = 2.95 mm. **g**,**h**, Imaging demonstration for a close object (d_o = 3 cm). The image captured with $d_{i,far}$ = 2.95 mm is blurry (**g**), but it can be refocused with $d_{i,3cm}$ = 4.72 mm (**h**). Inset: image of the original object.

In wide-FoV imaging, vignetting is a major issue in acquiring clear images. For example, light intensity after passing through a conventional wide-angle multi-lens is drastically attenuated in proportion to the fourth power of the cosine function of the incident angle[36]. Although the monocentric lens substantially corrects vignetting due to its spherical shape, the intensity of the passed light is still attenuated in proportion to the cosine function of the incident angle[36]. In addition, the thin flexible silicon photodiodes are accompanied by limited photo-absorption[37–39]. Accordingly, nanorod texturing and surface passivation are also applied to enhance the photo-absorption and light sensitivity of the photodiode.

Texturing is provided by a silicon nanorod array (Fig. 3d; see inset for an atomic force microscope (AFM) image and height profile), while a thin Al_2O_3 layer (~25 nm) is used to passivate the textured surface. Figure 3e presents a transmission electron microscope (TEM) image of the nanorods and passivation. The silicon nanorods (SiNRs) have a height of 220 nm, diameter of 200 nm and pitch of 520 nm. The parameters of the SiNRs were engineered according to a wave optics simulation (Supplementary Fig. 20). A large-scale TEM image showing the multiple SiNRs and energy-dispersive spectrometry (EDS) elemental distribution analyses showing the Al_2O_3 layer are provided in Supplementary Fig. 21.

The SiNRs show enhanced photo-absorption in visible spectra compared to bare silicon (Fig. 3f), because the nanorod-textured surface reduces surface reflection and transmission (Supplementary Fig. 22)[37,40]. Theoretical optical analyses show that the enhanced

photo-absorption of the SiNRs is due to a light trapping effect arising from diffraction at the nanorod structure (Supplementary Figs. 23 and 24). The incident light is diffracted by the nanorod-textured surface and trapped inside the SiNRs due to multiple total internal reflections. Thus, the overall light path for the photo-absorption is elongated[40]. More details of the theoretical optical analyses are provided in Supplementary Note 5.

The nanorod texturing of the silicon surface forms surface dangling bonds that generate a surface leakage current and thereby increase the dark current (I_{dark})[41]. Such surface dangling bonds also generate charge carrier recombination sites, which reduce the photocurrent (I_{photo})[40]. To combat this, surface passivation techniques have been used[39]. Here, Al_2O_3 passivation of the nanorod-textured silicon surface was applied; this suppresses the surface leakage current[41] and inhibits charge carrier recombination[40] by removing the dangling bonds and thus reduces I_{dark} and enhances I_{photo} (Fig. 3g). With these attributes, the SiNR photodiode with Al_2O_3 passivation can measure incident light with enhanced sensitivity (Fig. 3h). Figure 3i presents I–V curves of the SiNR photodiode with the Al_2O_3 passivation serially connected with the blocking diode under illumination of various light intensities, confirming the sensitive photoresponse of the SiNR photodiode as well as suppression of the reverse bias current by the blocking diode[13]. The dynamic range and photoresponsivity of the SiNR photodiode are as high as 61.2 dB and 0.34 A W^{-1}, respectively (Supplementary Fig. 25). In addition, the photoresponse speed of the SiNR photodiode is comparable to that of a bare silicon photodiode (Supplementary Fig. 26), and it can be improved further by exploiting a shorter intrinsic region length to reduce the transit time as well as by minimizing the parasitic resistance and capacitance[42,43].

Imaging demonstrations using the integrated camera module

Integration of the monocentric lens and the h-SiNR-PDA with a custom-made housing results in an aquatic-vision-inspired camera module. The camera module, its components and an exploded schematic illustration are presented in Fig. 4a, its inset and Supplementary Fig. 27, respectively. The aquatic-vision-inspired camera enables aberration-free wide-FoV imaging, but its module size (that is, optical axis length) is only 11.5 mm, which is comparable to the size of a quarter coin (Supplementary Fig. 28). Detailed specifications of the developed camera and those of commercial cameras and other bio-inspired imaging systems are summarized in Supplementary Table 6.

The aquatic-vision-inspired camera enables high-quality aberration-free imaging with wide FoV, deep DoF and facile accommodation, as shown in the optical analyses in Fig. 2. We validated these features with imaging demonstrations for objects located at wide angles and different distances. In the experimental set-up for the imaging demonstration, the position of the monocentric lens was fixed, while the positions of the h-SiNR-PDA and an object (patterned light passing through a shadow mask mounted on a light source) were adjusted using underlying rails. In this way, d_i and d_o could be controlled (Supplementary Fig. 29). The h-SiNR-PDA was connected to the external electronics via an anisotropic conductive film (ACF) and the photocurrent was measured using a customized data acquisition system (Supplementary Fig. 30). More details about the experimental set-up for the imaging demonstration and the data acquisition system with software algorithms are provided in Supplementary Note 6.

The aquatic-vision-inspired camera successfully performs various kinds of wide-FoV imaging without optical aberrations. Figure 4b shows a fish-shaped image captured by the aquatic-vision-inspired camera. The original object image is shown in the inset of Fig. 4b. The captured image is rendered on the hemispherical surface, whose radius matches the curvature of the h-SiNR-PDA. For quantitative validation of the aberration-free wide-FoV imaging, a cross pattern of spots located at various angles ranging between −60° and 60°, in 15° intervals (Fig. 4c, inset), was imaged by the h-SiNR-PDA. Each spot was imaged without distortion (Fig. 4c). The spots located on the outer side of the cross pattern could also be imaged well by using the pixels at the perimeter of the h-SiNR-PDA (corresponding to wide-FoV imaging). The FoV of the aquatic-vision-inspired camera could be improved up to 160° by using advanced lens manufacturing methods and by employing an image sensor array with a more hemispherical shape (Supplementary Fig. 31).

Because the spherical monocentric lens reduces vignetting and the h-SiNR-PDA exhibits enhanced sensitivity, the aquatic-vision-inspired camera allows us to capture images in a dim environment. Figure 4d shows square patterns captured under different light intensities. The dim square pattern with an intensity of only 0.040 W m^{-2} is imaged well. In addition, the aquatic-vision-inspired camera can perform imaging in the near-infrared (NIR), as the SiNR can absorb NIR light ($\lambda = 850$ nm; Fig. 4e). A photograph of the original NIR object is shown in the inset of Fig. 4e.

The aquatic-vision-inspired camera also features a deep DoF due to its inherently short d_f. All objects located at 20 cm or more can be imaged with a single $d_{i,far} = 2.95$ mm (Supplementary Fig. 32). In another case, two objects (a triangle (object 1) and a square (object 2)) placed at different distances ($d_{o,1} = 20$ cm and $d_{o,2} = 30$ cm) and at different angles with 90° difference (Supplementary Fig. 33) can be simultaneously imaged with a single $d_{i,far} = 2.95$ mm (Fig. 4f). However, if an object located at a close position (for example, $d_o = 3$ cm, Fig. 4g, inset) is to be imaged with $d_{i,far}$, the captured image becomes blurry due to the increased d_f for $d_o = 3$ cm (Fig. 4g). In this case, visual accommodation is needed. The position of the h-SiNR-PDA is adjusted to change d_i to match the increased $d_{f,3cm} = 4.72$ mm. The blurry image of the letter 'E' captured with $d_{i,far} = 2.95$ mm (Fig. 4g) can then be refocused with an adjusted $d_{i,3cm} = 4.72$ mm (Fig. 4h).

Conclusions

Inspired by natural aquatic-vision systems, we have developed a miniaturized wide-FoV camera by integrating a monocentric lens with an h-SiNR-PDA. Our camera features a wide FoV, miniaturized design, minimum optical aberration, deep DoF, simple visual accommodation and enhanced light sensitivity. The entire system is enclosed in a single small-form-factor unit, and is fabricated using accessible laboratory-based methods. The aquatic-vision-inspired camera could be of use in a number of emerging technological applications, particularly where obstacle avoidance and object tracking at wide angles is required, and could help expand the current capabilities of advanced mobile electronic devices.

Methods

Fabrication of the monocentric lens and its detailed specifications. To fabricate the monocentric lens, two kinds of lens (BK7 and SF16) were used. The RI (at a wavelength of 588 nm) and RoC of BK7 are 1.52 and 2 mm and those of SF16 are 1.65 and 4.1 mm, respectively. A transparent optical adhesive (NOA 61, Norland Products) with RI of 1.56 was used to fill the space between the lenses. The surface profile of each lens was analysed using a large-area aspheric 3D profiler (UA3P, Panasonic).

Fabrication of the monocentric lens (Supplementary Fig. 8) began with drop-coating of NOA 61 on the half-ball lens (BK7; Edmund Optics). The half-ball lens was then aligned on the aperture using an automated centring machine, and NOA 61 was cured by ultraviolet irradiation to fix the half-ball lens with the aperture. The space between the half-ball lens and the aperture was filled with NOA 61, and another half-ball lens was placed on the opposite side of the aperture and fixed by ultraviolet curing of the NOA 61. The shell lenses (SF16) were pre-fabricated by a direct single-point diamond turning method with post-polishing. NOA 61 was then drop-coated on the half-ball lens, the shell lens was placed on the half-ball lens, and the half-ball lens and the shell lens were fixed by ultraviolet curing of the NOA 61. The ledge on the aperture allowed precise alignment between the aperture and the shell lens. The surface profile of the aperture and the shell lens is shown in Supplementary Fig. 34. The surface profiles

were measured using a non-contacting 3D surface profile measurement device (NH-3SPs, Mitaka Kohki). Repeating the same procedure (assembling another shell lens on the other side of the aperture) completed the fabrication of the monocentric lens.

Fabrication and characterization of the h-SiNR-PDA. Fabrication of the h-SiNR-PDA began with spin-coating of a polystyrene (PS) microsphere (diameter of 0.5 μm; Thermo Fisher Scientific) solution on a silicon-on-insulator wafer (1.25-μm-thick top silicon; SOITEC). A series of dry etching processes with oxygen and SF_6 formed the SiNR textured surface[44]. The residual PS microspheres were removed by sonication and piranha solution treatment. A series of doping processes were performed by using spin-on dopants. The SiNR nanomembrane was spin-coated with n-type spin-on-dopant (P509 solution; Filmtronics) and annealed at 200 °C for 15 min and at 975 °C for 12 min for n-doping, and then was spin-coated with the p-type spin-on dopant (B153 solution; Filmtronics) and annealed at 200 °C for 15 min and at 975 °C for 30 min for p-doping. The doping profiles were analysed by magnetic sector secondary ion mass spectrometry (IMS 7f, CAMECA; Supplementary Fig. 35). The nanorod-textured and doped silicon nanomembrane was transfer-printed onto the polyimide (PI) bottom substrate film (~1 μm thick; Sigma Aldrich) spin-coated on a SiO_2 wafer. The active silicon diode region was isolated using photolithography and dry etching, then the Al_2O_3 passivation layer (~25 nm) was deposited by the plasma-enhanced atomic layer deposition and isolated through photolithography and wet etching using a buffered oxide etchant. An additional PI film for the first intermediate dielectric (~1 μm thick) was spin-coated and cured. The via was patterned by photolithography and dry etching, and Cr/Au layers for first metal electrode (10/100 nm) were deposited and patterned by thermal evaporation and wet etching, respectively. Additional spin-coating and curing of the PI film for the second intermediate dielectric (~1 μm thick) and deposition of Cr/Au layers for the second metal electrode (10/100 nm) were performed using the same process. A final PI film for top encapsulation (~1 μm thick) was spin-coated and cured, then the entire PI film was etched into a hexagonal mesh structure by dry etching. The fabricated h-SiNR-PDA was detached from the SiO_2 wafer using a water-soluble tape (3M Corp.) and transfer-printed onto a hemispherically curved substrate made of polydimethylsiloxane (Dow Corning).

The individual pixel, that is, a photodiode serially connected to a blocking diode (lateral n–p–n configuration), was used for characterization. A white light-emitting diode was used as a light source. For device characterization, the photocurrents of the experimental and control devices (for example, the SiNR photodiode with and without Al_2O_3 passivation) were measured using a parameter analyser (B1500A, Agilent). Outlier data (the largest and smallest) were excluded.

Data availability

The data that support the plots within this paper and other findings of this study are available from the corresponding author upon reasonable request.

Code availability

The source codes for Matlab are available from the corresponding authors upon request.

Received: 29 November 2019; Accepted: 28 May 2020;
Published online: 22 June 2020

References

1. Floreano, D. & Wood, R. J. Science, technology and the future of small autonomous drones. *Nature* **521**, 460–466 (2015).
2. Jang, H. S. et al. A bezel-less tetrahedral image sensor formed by solvent-assisted plasticization and transformation of an acrylonitrile butadiene styrene framework. *Adv. Mater.* **30**, 1801256 (2018).
3. Lee, G. J., Choi, C., Kim, D.-H. & Song, Y. M. Bioinspired artificial eyes: optic components, digital cameras and visual prostheses. *Adv. Funct. Mater.* **28**, 1705202 (2018).
4. Chung, T. et al. Mining the smartness of insect ultrastructures for advanced imaging and illumination. *Adv. Funct. Mater.* **28**, 1705912 (2018).
5. Lee, G. J., Nam, W. I. & Song, Y. M. Robustness of an artificially tailored fisheye imaging system with a curvilinear image surface. *Opt. Laser Technol.* **96**, 50–57 (2017).
6. Zhou, F. et al. Optoelectronic resistive random access memory for neuromorphic vision sensors. *Nat. Nanotechnol.* **14**, 776–782 (2019).
7. Lee, W. et al. Two-dimensional materials in functional three-dimensional architectures with applications in photodetection and imaging. *Nat. Commun.* **9**, 1417 (2018).
8. Tsai, W.-L. et al. Band tunable microcavity perovskite artificial human photoreceptors. *Adv. Mater.* **31**, 1900231 (2019).
9. Choi, C. et al. Human eye-inspired soft optoelectronic device using high-density MoS_2–graphene curved image sensor array. *Nat. Commun.* **8**, 1664 (2017).
10. Zhang, K. et al. Origami silicon optoelectronics for hemispherical electronic eye systems. *Nat. Commun.* **8**, 1782 (2017).
11. Ko, H. C. et al. A hemispherical electronic eye camera based on compressible silicon optoelectronics. *Nature* **454**, 748–753 (2008).
12. Artal, P. Optics of the eye and its impact in vision: a tutorial. *Adv. Opt. Photon.* **6**, 340–367 (2014).
13. Song, Y. M. et al. Digital cameras with designs inspired by the arthropod eye. *Nature* **497**, 95–99 (2013).
14. Floreano, D. et al. Miniature curved artificial compound eyes. *Proc. Natl Acad. Sci. USA* **110**, 9267–9272 (2013).
15. Jeong, K.-H., Kim, J. & Lee, L. P. Biologically inspired artificial compound eyes. *Science* **312**, 557–561 (2006).
16. Huang, C.-C. et al. Large-field-of-view wide-spectrum artificial reflecting superposition compound eyes. *Small* **10**, 3050–3057 (2014).
17. Jagger, W. S. & Sands, P. J. A wide-angle gradient index optical model of the crystalline lens and eye of the rainbow trout. *Vis. Res.* **36**, 2623–2639 (1996).
18. Jagger, W. S. & Sands, P. J. A wide-angle gradient index optical model of the crystalline lens and eye of the octopus. *Vis. Res.* **39**, 2841–2852 (1999).
19. Mass, A. M. & Supin, A. Y. Adaptive features of aquatic mammals' eye. *Anat. Rec.* **290**, 701–715 (2007).
20. Charman, W. N. & Tucker, J. The optical system of the goldfish eye. *Vis. Res.* **13**, 1–8 (1973).
21. Ott, M. Visual accommodation in vertebrates: mechanisms, physiological response and stimuli. *J. Comp. Physiol. A* **192**, 97–111 (2006).
22. Wagner, H.-J., Frohlich, E., Negishi, K. & Collin, S. P. The eyes of deep-sea fish. II. Functional morphology of the retina. *Prog. Retin. Eye Res.* **17**, 637–685 (1998).
23. Partridge, J. C., Archer, S. N. & Lythgoe, J. N. Visual pigments in the individual rods of deep-sea fishes. *J. Comp. Physiol. A* **162**, 543–550 (1988).
24. Wu, T. et al. Design and fabrication of silicon-tessellated structures for monocentric imagers. *Microsyst. Nanoeng.* **2**, 16019 (2016).
25. Liu, H. W., Huang, Y. & Jiang, H. Artificial eye for scotopic vision with bioinspired all-optical photosensitivity enhancer. *Proc. Natl Acad. Sci. USA* **113**, 3982–3985 (2016).
26. Zukauskas, A. et al. Tuning the refractive index in 3D direct laser writing lithography: towards GRIN microoptics. *Laser Photon. Rev.* **9**, 706–712 (2015).
27. Yu, N. & Capasso, F. Flat optics with designer metasurfaces. *Nat. Mater.* **13**, 139–150 (2014).
28. Steel, W. H. On the choice of glasses for cemented achromatic aplanatic doublets. *Aust. J. Phys.* **7**, 244–253 (1954).
29. Lee, W. et al. High-resolution spin-on-patterning of perovskite thin films for a multiplexed image sensor array. *Adv. Mater.* **29**, 1702902 (2017).
30. Sim, K. et al. Three-dimensional curvy electronics created using conformal additive stamp printing. *Nat. Electron.* **2**, 471–479 (2019).
31. Shin, G. et al. Micromechanics and advances designs for curved photodetector arrays in hemispherical electronic-eye cameras. *Small* **6**, 851–856 (2010).
32. Huang, Z. et al. Three-dimensional integrated stretchable electronics. *Nat. Electron.* **1**, 473–480 (2018).
33. Park, S.-I. et al. Theoretical and experimental studies of bending of inorganic electronic materials on plastic substrates. *Adv. Funct. Mater.* **18**, 2673–2684 (2008).
34. Choi, M. K. et al. Wearable red-green-blue quantum dot light-emitting diode array using high-resolution intaglio transfer printing. *Nat. Commun.* **6**, 7149 (2015).
35. Kim, J. et al. Stretchable silicon nanoribbon electronics for skin prosthesis. *Nat. Commun.* **5**, 5747 (2014).
36. Rim, S.-B., Catrysse, P. B., Dinyari, R., Huang, K. & Peumans, P. The optical advantages of curved focal plane arrays. *Opt. Express* **16**, 4965–4971 (2008).
37. Sheng, X., Johnson, S. G., Michel, J. & Kimerling, L. C. Optimization-based design of surface textures for thin-film Si solar cells. *Opt. Express* **19**, A841–A850 (2011).
38. Sheng, X. et al. Printing-based assembly of quadruple-junction four-terminal microscale solar cells and their use in high-efficiency modules. *Nat. Mater.* **13**, 593–598 (2014).
39. Hoang, N.-V. et al. Giant enhancement of luminescence down-shifting by a doubly resonant rare-earth-doped photonic metastructure. *ACS Photonics* **4**, 1705–1712 (2017).
40. Savin, H. et al. Black silicon solar cells with interdigitated back-contacts achieve 22.1% efficiency. *Nat. Nanotechnol.* **10**, 624–628 (2015).
41. Gao, Y. et al. Photon-trapping microstructures enable high-speed high-efficiency silicon photodiodes. *Nat. Photon.* **11**, 301–308 (2017).
42. Lucovsky, G., Schwarz, R. F. & Emmons, R. B. Transit-time considerations in p–i–n diodes. *J. Appl. Phys.* **35**, 622–628 (1964).
43. Kyomasu, Mikio Development of an integrated high speed silicon PIN photodiode sensor. *IEEE Trans. Electron Devices* **42**, 1093–1099 (1995).
44. Gao, M., Cho, M., Han, H.-J., Jung, Y. S. & Park, I. Palladium-decorated silicon nanomesh fabricated by nanosphere lithography for high performance, room temperature hydrogen sensing. *Small* **14**, 1703691 (2018).

Acknowledgements

This research was supported by the Institute for Basic Science (IBS-R006-A1). This research was also supported by the National Research Foundation (NRF) of Korea (2017M3D1A1039288/2018R1A4A1025623).

Author contributions

M.K., G.J.L., C.C., M.S.K., K.W.C., Y.M.S. and D.-H.K. designed the experiments, analysed the data and wrote the paper. M.S.K., C.C., M.L., H.C. and M.K.C. fabricated the photodiode array and performed characterization of individual devices. G.J.L., M.S.K. and H.M.K. performed theoretical analysis on optics. S.L. and N.L. performed theoretical analysis on mechanics. All authors discussed the results and commented on the manuscript.

Competing interests

The authors declare no competing interests.

Additional information

Supplementary information is available for this paper at https://doi.org/10.1038/s41928-020-0429-5.

Correspondence and requests for materials should be addressed to Y.M.S. or D.-H.K.

Reprints and permissions information is available at www.nature.com/reprints.

Publisher's note Springer Nature remains neutral with regard to jurisdictional claims in published maps and institutional affiliations.